

# Sensing individual nuclear spins with a single rare-earth electron spin

Thomas Kornher,<sup>1,\*</sup> Da-Wu Xiao,<sup>2</sup> Kangwei Xia,<sup>1</sup> Fiammetta Sardi,<sup>1</sup> Nan Zhao,<sup>2</sup> Roman Kolesov,<sup>1</sup> and Jörg Wrachtrup<sup>1</sup>

<sup>1</sup>*3rd Institute of Physics, University of Stuttgart, 70569 Stuttgart, Germany*

<sup>2</sup>*Beijing Computational Science Research Center, Haidian District, Beijing 100194, China*

Rare-earth related electron spins in crystalline hosts are unique material systems, as they can potentially provide a direct interface between telecom band photons and long-lived spin quantum bits. Specifically, their optically accessible electron spins in solids interacting with nuclear spins in their environment are valuable quantum memory resources. Detection of nearby individual nuclear spins, so far exclusively shown for few dilute nuclear spin bath host systems such as the NV center in diamond or the silicon vacancy in silicon carbide, remained an open challenge for rare-earths in their host materials, which typically exhibit dense nuclear spin baths. Here, we present the electron spin spectroscopy of single  $\text{Ce}^{3+}$  ions in a yttrium orthosilicate host, featuring a coherence time of  $T_2 = 124 \mu\text{s}$ . This coherent interaction time is sufficiently long to isolate proximal  $^{89}\text{Y}$  nuclear spins from the nuclear spin bath of  $^{89}\text{Y}$ . Furthermore, it allows for the detection of a single nearby  $^{29}\text{Si}$  nuclear spin, native to the host material with ~5 % abundance. This study opens the door to quantum memory applications in rare-earth ion related systems based on coupled environmental nuclear spins, potentially useful for quantum error correction schemes.

Hybrid quantum systems, consisting of a read-out electron spin and long-lived nuclear spins, have demonstrated remarkable properties for quantum memory applications [1–3]. At the same time single spins enable active quantum processing used in e.g. quantum error correction [4]. Implementing them in scalable quantum networks based on single rare-earth ions (REI) doped in solids potentially combines long distance entanglement distribution via single telecom band photons[5] with error corrected long-lived quantum memories.

Based on the efficient isolation of REI's  $4f$  electrons, their narrow and stable optical and spin levels have been used for demonstration of storage and retrieval of single photons [6] and exceptional coherence times [7], rendering them particularly suitable for quantum repeater protocols. With additional control over single rare-earth ions, however, these capabilities can be extended to high-fidelity spin readout and generation of entanglement of rare-earth electrons and nuclei in a scalable fashion[3]. Consequently, an increasing number of REI are isolated as single emitters [5, 8–11]. Based on ancillary electron spins of these single emitters, sensing of nuclear spins [12–16] is an important next step for REI based quantum network applications. So far, only dilute nuclear spin bath host materials such as diamond [17], silicon carbide [18] and silicon [19] were successfully used for detection of individual nuclear spins.

In this study, we use the yttrium orthosilicate ( $\text{Y}_2\text{SiO}_5$ , YSO) crystal to investigate the nuclear environment of individual  $\text{Ce}^{3+}$  electron spins, which simultaneously act as a proxy for other REI species, owing to their interchangeable doping into yttrium containing solids. We demonstrate spin initialization and coherent manipulation of  $\text{Ce}^{3+}$  electron spins in a YSO host crystal. Surprisingly we were able to sense individual dipolar coupled  $^{29}\text{Si}$  nuclear spins despite the strong yttrium spin bath.

$^{29}\text{Si}$  signal is distilled furthermore with basic decoupling sequences. Signatures of yttrium nuclear spins also reveal dipolar coupling with the nearby  $\text{Ce}^{3+}$  superimposed on the yttrium spin bath.

Trivalent cerium substitutes  $\text{Y}^{3+}$  in 95 % of the cases at the 7-oxygen-coordinated site of the YSO crystal with a  $C_1$  symmetry [20]. The remaining 5 % of  $\text{Ce}^{3+}$  ions substituting  $\text{Y}^{3+}$  in the 6-oxygen-coordinated site of the crystal can be neglected from further considerations due to different optical (red shifted) and magnetic (different g-tensor) properties [20, 21]. Individual  $\text{Ce}^{3+}$  ions were identified in an ultra-pure YSO crystal using laser scanning confocal microscopy. The experimental setup of the microscope is described in detail in the supplementary material [22]. To improve the collection efficiency and spatial resolution of the microscope, solid immersion lenses (SIL) were fabricated on the surface of the sample by focused ion beam milling. A scanning electron microscopy (SEM) image of the sample with milled SILs and an indicated wire used for microwave (MW) spin manipulation is shown in Fig. 1a. A picosecond pulsed laser at 355 nm wavelength was used to off-resonantly excite  $\text{Ce}^{3+}$  ions from the  $4f$  ground state into the excited  $5d$  band based on their phonon-assisted absorption band [21]. The corresponding energy level structure of  $\text{Ce}^{3+}$  in YSO is shown in Fig. 1b. For the purpose of acquiring a fluorescence spectrum,  $5d \rightarrow 4f$  emission was collected from a 0.01% doped  $\text{Ce}^{3+}$ :YSO crystal at  $T \approx 8 \text{ K}$  (inset Fig. 1d). A high resolution spectrum of  $\text{Ce}^{3+}$ :YSO, shown in Fig. 1d, reveals the zero-phonon line at 371 nm, characteristic for  $\text{Ce}^{3+}$  ion fluorescence at cryogenic temperatures [23]. Performing confocal microscopy with the pulsed 355 nm laser on the SILs, however, allows for resolving individual  $\text{Ce}^{3+}$  ions. A typical laser scanning fluorescence image of optically resolved  $\text{Ce}^{3+}$  ions located in the focus of a SIL is shown in Fig. 1c.

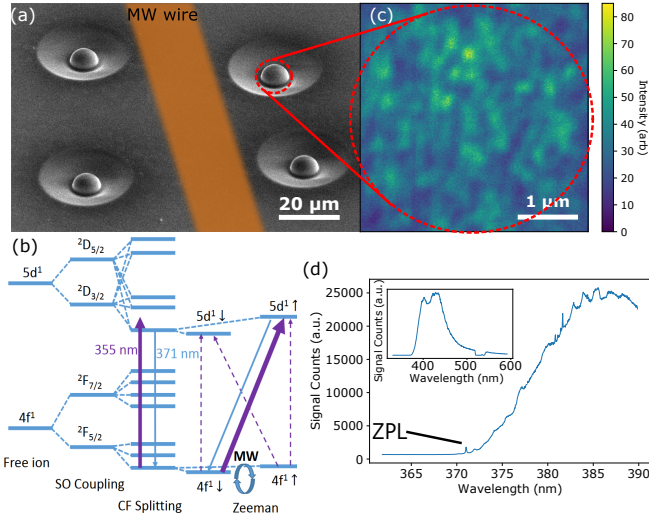


FIG. 1. (a) SEM image of SILs on a YSO crystal surface. The MW copper wire position is indicated by an orange stripe. (b) Electronic level structure of  $\text{Ce}^{3+}$  ion in YSO crystal. Purple arrows indicate laser excitation and blue arrows fluorescence. Under circularly polarized excitation light, directed along the same axis as the applied external magnetic field (along the  $b$  axis of the crystal), different strengths of optical transitions between the lowest  $4f$  level and the lowest  $5d$  level are indicated by different widths of arrows. (c) Confocal scan of cerium centers under pulsed laser excitation, taken at the focus of a SIL. (d) High-resolution spectrum of the zero-phonon line at 371 nm. Inset: Typical spectrum of a 0.01 %  $\text{Ce}^{3+}$ :YSO crystal at 8 K. The gap in the spectrum around 532 nm is an artifact of the used notch filter.

Even in ultra-pure crystals (from Scientific Materials), cerium is an unavoidable native impurity for yttrium-based hosts and the estimated residual density of 0.3 ppb in our crystal is the main contribution to background signal and can result in more than one  $\text{Ce}^{3+}$  ion to be probed within the focal volume. In principle, stimulated emission depletion (STED) based superresolution microscopy is available for  $\text{Ce}^{3+}$ :YSO (see supplementary material [22]) [24], however the spin initialization and readout was found to be prevented by the high power depletion laser used in the experiment.

In a magnetic field parallel to the optical excitation beam, optical transitions between  $4f^1$  and  $5d^1$  spin doublets show different relative strengths under  $\sigma^+$  circularly polarized excitation [10]. While the  $|4f^1 \downarrow\rangle \rightarrow |5d^1 \uparrow\rangle$  spin-flip transition exhibits the strongest optical dipole moment out of the four possible transitions under  $\sigma^+$  circularly polarized excitation (indicated in Fig. 1b), the radiative decay originating from the excited  $5d^1$  level ends up in both ground state spin levels with equal probability. A repeated excitation of the selectively driven spin-flip transition eventually results in a polarized ground state spin level. When applying the optical polarization

procedure, the spin is pumped into the optically 'dark' state[25], which results in a reduced fluorescence signal. MW radiation resonant with the ground  $4f^1$  state spin transition can then be used to flip the optically polarized spin. This results in an increased fluorescence signal, which allows for optically detected magnetic resonance (ODMR) measurements on individual cerium ions.

Initialization measurements, shown in Fig. 2a., capture the dynamic evolution of the fluorescence signal as a function of the laser pulse number. Starting with a thermal polarization, the fluorescence signal drops with increasing number of laser pulses because of optical pumping of the spin. Initialization fidelities range between 5% and 15%, depending on the individual  $\text{Ce}^{3+}$  ion under investigation. The relatively high background of densely packed  $\text{Ce}^{3+}$  ions in the sample can contribute to measuring a decreased fidelity.

In our experiments, a magnetic field with a strength of 970 Gauss was applied parallel to the optical beam and the  $b$ -axis of the YSO crystal, for which  $\text{Ce}^{3+}$  has a  $g$ -factor of  $g_{\text{Ce}} \approx 1.4$  and a magnetic resonance frequency of 1930.5 MHz[20]. MW structures created in proximity of SILs were then used to sweep the MW radiation frequency in order to observe ODMR spectra of individual  $\text{Ce}^{3+}$  ions. A typical spectrum is shown in Fig. 2b and exhibits a linewidth of 2-3 MHz, slightly different for different cerium ions.

Coherent  $\text{Ce}^{3+}$  spin manipulation is demonstrated in a measurement of spin Rabi oscillations under strong MW driving, shown in Fig. 2c. A typical sequence for such a Rabi measurement contains spin initialization, control and readout, as shown in the inset of Fig. 2c. An exponentially decaying sine function was fitted to the Rabi measurement signal, revealing a Rabi frequency of 5.6 MHz and a decay time of  $2 \mu\text{s}$ .

A free induction decay (FID) experiment is capable to reveal the electron spin coherence in the thermal noise of the characteristic nuclear spin bath of YSO, featuring  $^{89}\text{Y}$  and  $^{29}\text{Si}$  nuclear spins. Fig. 2d presents a typical FID of  $\text{Ce}^{3+}$  and quantifies the inhomogeneous broadening of  $\text{Ce}^{3+}$  spin transition to  $T_2^* = 310 \text{ ns}$ , by fitting with a Gaussian. These dephasing times are in good agreement with ODMR linewidth measurements. The main contribution to inhomogeneous broadening may emerge from the nuclear spin bath and can also come from short-pulsed optical excitation of  $\text{Ce}^{3+}$ , causing ionization of electron traps nearby the electron spin, which induce charge fluctuations capable of stark-shifting the resonance.

The Hahn spin echo sequence decouples the spin from slow (compared to  $\tau$ ) changes in the environment and allows for more detailed spin spectroscopy of the nuclear spin environment of  $\text{Ce}^{3+}$  electron spins. A representative Hahn echo measurement on  $\text{Ce}^{3+}$  is shown in Fig. 3a. We observe periodic revivals related to yttrium ions in the crystal, which have 100% abundance of nuclear spin  $I_Y = 1/2$  with magnetic moment  $\mu_Y = -0.137 \mu_N$ ,

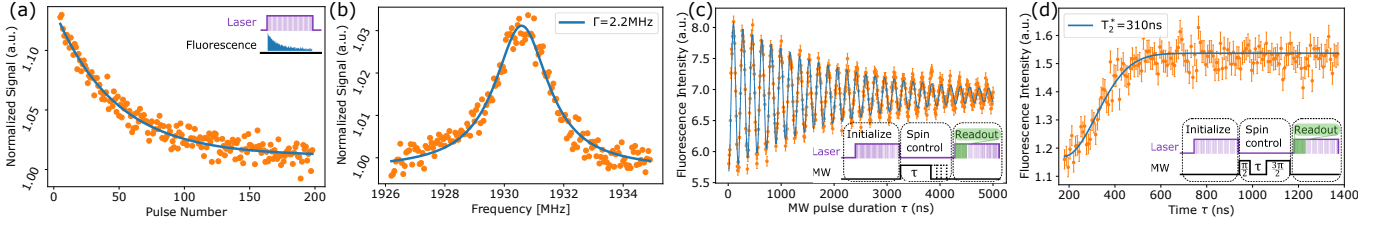


FIG. 2. a) Fluorescence intensity as function of the laser pulse number during initialization. For coherent spin manipulation experiments, 100 pulses were used for spin initialization. b) ODMR measurement of  $\text{Ce}^{3+}$  as a function of MW frequency. A fitted Lorentzian reveals a linewidth of 2.2 MHz. c)  $\text{Ce}^{3+}$  spin Rabi oscillations. Blue line is a fit to the data with an exponentially decaying cosine function with constant offset. d) Ramsey measurement of  $\text{Ce}^{3+}$  with Gaussian fit yielding  $T_2^* = 310 \text{ ns}$ .

with  $\mu_N$  as the nuclear magneton. The overall decaying signal corresponds to a decoherence time of  $T_2 = 124 \mu\text{s}$  and was fitted to  $\exp[-(2\tau/T_2)^3]$  [17]. Based on the cluster-correlation expansion method [27], the coherence of the electron spin in an interacting bath is simulated and plotted as blue line in Fig. 3a. For the  $\text{Ce}^{3+}$  electron spin located in a complex nuclear environment such as the YSO matrix, the simulated behaviour of its coherence under spin echo control agrees strikingly well with our experimental results. Details of the simulations are described in the supplementary material [22]. The Fast Fourier Transform (FFT) of the Hahn echo signal (see Fig. 3b) reveals two particular facts. Firstly, yttrium bath related signatures, found at the Larmor precession frequency  $\omega_{Y, \text{Larmor}} \approx 200 \text{ kHz}$ , similarly known from single NV centers in diamond [17]. Additionally, we find frequency components related to weakly coupled yttrium nuclear spins based on magnetic dipole interaction with the electron spin. The measured hyperfine coupling strengths are in good agreement with simulated splittings (in the range between 50 kHz and 120 kHz).

We measured the lifetime of the spin state  $T_1$  after optical initialization by reading out the spin state after a variable waiting time  $\tau$ . The spin relaxation measurements are shown in Fig. 3c and reveal  $T_1 = 610 \mu\text{s}$  at a temperature of  $T = 3.8 \text{ K}$ , measured at the heat exchanger of our cold-finger cryostat. At an indicated temperature of  $T = 4.5 \text{ K}$ , the spin lattice relaxation measurement yields  $T_1 = 280 \mu\text{s}$ . By comparing our measured  $T_1$  values with EPR based values [28], we can identify the actual sample temperatures to be approximately 4 K higher than measured on the heat exchanger, because of insufficient cooling power.

Using confocal microscopy, we can study spatially resolved  $\text{Ce}^{3+}$  ions and their unique environment. For each silicon ion in the crystal lattice, there is a 4.7 % natural abundance of  $^{29}\text{Si}$  isotope with a nuclear spin  $I_{\text{Si}} = 1/2$  and  $\mu_Y = -0.555 \mu_N$ . For a  $\text{Ce}^{3+}$  ion under investigation, this leads to a chance of approximately 20 % to have a  $^{29}\text{Si}$  as nearest neighbor. At the nearest neighbor location, the close distance ( $\leq 6 \text{ \AA}$ ) between electron spin and  $^{29}\text{Si}$  nuclear spin leads to a detectable hyperfine coupling

based on magnetic dipole interaction, superimposed on the hyperfine interaction with closeby yttrium spins and the yttrium bath (schematically shown in Fig. 4a).

Dynamic decoupling (DD) of the  $\text{Ce}^{3+}$  spin from the nuclear bath allows to extract  $^{29}\text{Si}$  related signatures. Carr-Purcell-Meiboom-Gill (CPMG) control sequences were used to acquire noise spectra for two different  $\text{Ce}^{3+}$  ions, as shown in Fig. 4(b)-(d). The center of the coherence dip (in Fig. 4b and inset) at  $\tau_{\text{dip}} \approx 600 \text{ ns}$ , corresponds to a revival time of  $\tau_r = 2\tau_{\text{dip}}$ .  $1/\tau_r$  matches well with the gyromagnetic ratio  $\gamma_{\text{Si}} = -8.465 \text{ MHz/T}$ , thus confirming the nearby  $^{29}\text{Si}$  nuclear spin. Specifically, CPMG- $N$  decoupling sequences were used, with  $N = 1, 2, 5$  denoting the number of  $\pi$  pulses used in the sequences. The bandwidth depends on the number of pulses and scales approximately with  $f/(N/2)$  at frequency  $f = 1/2\tau$ . [29]. With an increasing number  $N$  of  $\pi$  pulses, the noise filter function causes the  $^{29}\text{Si}$  signature to be split in  $N$  coherence dips. This can be seen in the insets of Fig. 4(b)-(d), where the  $^{29}\text{Si}$  signal is isolated by plotting the difference between signals from the two  $\text{Ce}^{3+}$  ions under investigation. Solid lines in Fig. 4 are simulated noise spectra of  $\text{Ce}^{3+}$  ions located in a specific nuclear spin environment. In order to account for differences in the depth of coherence dips between experiment and simulation, we phenomenologically add a relaxation and dephasing mechanism to the dynamics of  $^{29}\text{Si}$  (see [22]). One possible reason for a reduced depth of the coherence dip in the experiment is external noise for proximal  $^{29}\text{Si}$ . Broadening mechanisms can be related to magnetic field fluctuations introduced by MW manipulation of  $\text{Ce}^{3+}$ , the optical initialization as described for the NV center system [30] or residual RE Kramers ion impurities in the crystal (such as  $\text{Er}^{3+}$ ,  $\text{Gd}^{3+}$ , ...), acting as a noise source on a short timescale.

Based on our simulations, we can localize a coupled  $^{29}\text{Si}$  nuclear spin within the nearest neighbor position in the lattice ("ion B", magenta). Furthermore, the comparison spectrum without  $^{29}\text{Si}$  nuclear spin signatures ("ion A", blue) reveals information about the absence of  $^{29}\text{Si}$  within 6 Å distance from the  $\text{Ce}^{3+}$  ion. The probability to find a  $\text{Ce}^{3+}$  ion with the same nuclear spin environ-

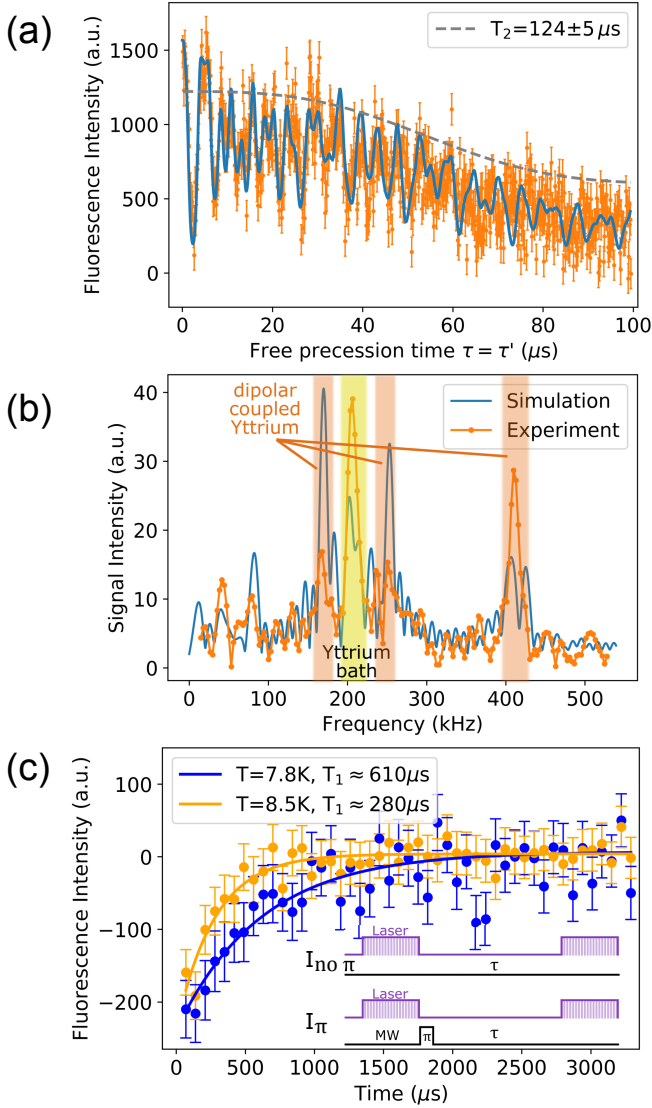


FIG. 3. a) Hahn echo measurement shows collapse and revivals. The decay is fitted to  $\exp[-(2\tau/T_2)^3]$  (grey dashed line), with  $T_2 \approx 124 \mu\text{s}$ , plotted offset on the intensity axis to envelope the signal. Simulated coherence is plotted as blue continuous line. b) FFT of the Hahn-Echo signal (orange) and FFT of the simulated Hahn-Echo signal (blue). Highlighted in yellow is the yttrium bath contribution at  $\approx 200$  kHz. Highlighted in orange are the contributions originating from dipolar coupled yttrium nuclear spins in close proximity to  $\text{Ce}^{3+}$  [26]. c) Spin relaxation measurement shows  $T_1 = 610 \mu\text{s}$  and  $T_1 = 280 \mu\text{s}$  for sample temperatures of 7.8 K and 8.5 K. Signal is the difference between the two sequences, indicated in the inset.

ment as "ion A" in YSO is  $\sim 70\%$ .

In conclusion, we show coherent control of an individual  $\text{Ce}^{3+}$  electron spin in a YSO matrix. Using spin decoupling techniques, our spin spectroscopy reveals the single REI electron spin to be dipolar coupled to nearby nuclear spins. Based on high density of yttrium in the

host crystal, the future challenge is to distinguish spectrally between individual coupled nuclear spins. Carefully designed DD sequences can improve detection of nuclear spin signals, which tend to be submerged by the noisy spin bath [31].  $^{29}\text{Si}$  nuclear spin sensing was demonstrated, for  $^{29}\text{Si}$  being located within the nearest neighbor shell.

Nuclear spins (either  $^{29}\text{Si}$  nuclear spin or yttrium nuclear spin) in proximity to the  $\text{Ce}^{3+}$  electron spin are quantum resources for quantum memory protocols. By establishing polarization transfer techniques, for example based on Hartmann-Hahn double resonance techniques [32], single  $^{29}\text{Si}$  nuclear spin could be initialized and potentially used as memory. A key concern is the coherence time of nuclear spins in this context. Decoherence caused by the nuclear spin bath will set the ultimate limitation for the coherence time. Due to weak dipolar interaction between nuclear spins in YSO compared to the Zeeman energy at applied magnetic fields, only the pure-dephasing interaction can have significant effect on the decoherence [27]. The characteristic decoherence time scale can be estimated by the nuclear spin dipolar interaction and gives  $T_2^* \sim 10$  ms for  $^{29}\text{Si}$  nuclear spin and  $T_2^* \sim 50$  ms for yttrium nuclear spin.

Finally, this work motivates the realization of controllable multispin quantum registers based on single REIs embedded in the YSO matrix. Access to local nodes based on environmental spins, as demonstrated in [4], provides functionality of quantum memories, such as error correction. Furthermore, presented findings are applicable to other Kramers ions doped into YSO, such as erbium, for which coherent spin control and readout was demonstrated recently [33].

R.K. acknowledges financial support by the DFG (Grant No. KO4999/3-1) and R.K. and J.W. acknowledge financial support by the FET-Flagship Project SQUARE, the EU via SMeL and QIA as well as the DFG via FOR 2724. N.Z. acknowledges financial support by NSFC (Grant No. 11534002) and NSAF (Grant No. U1530401 and Grant No. U1730449).

## Supplementary Information

### LASER SCANNING CONFOCAL MICROSCOPE SETUP

The experiment was carried out in a cold-finger cryostat (CryoVac, KONTI-CRYOSTAT TYPE MICRO), where the sample is mounted on top of a permanent magnet, which is mounted on the cold-finger (sketch



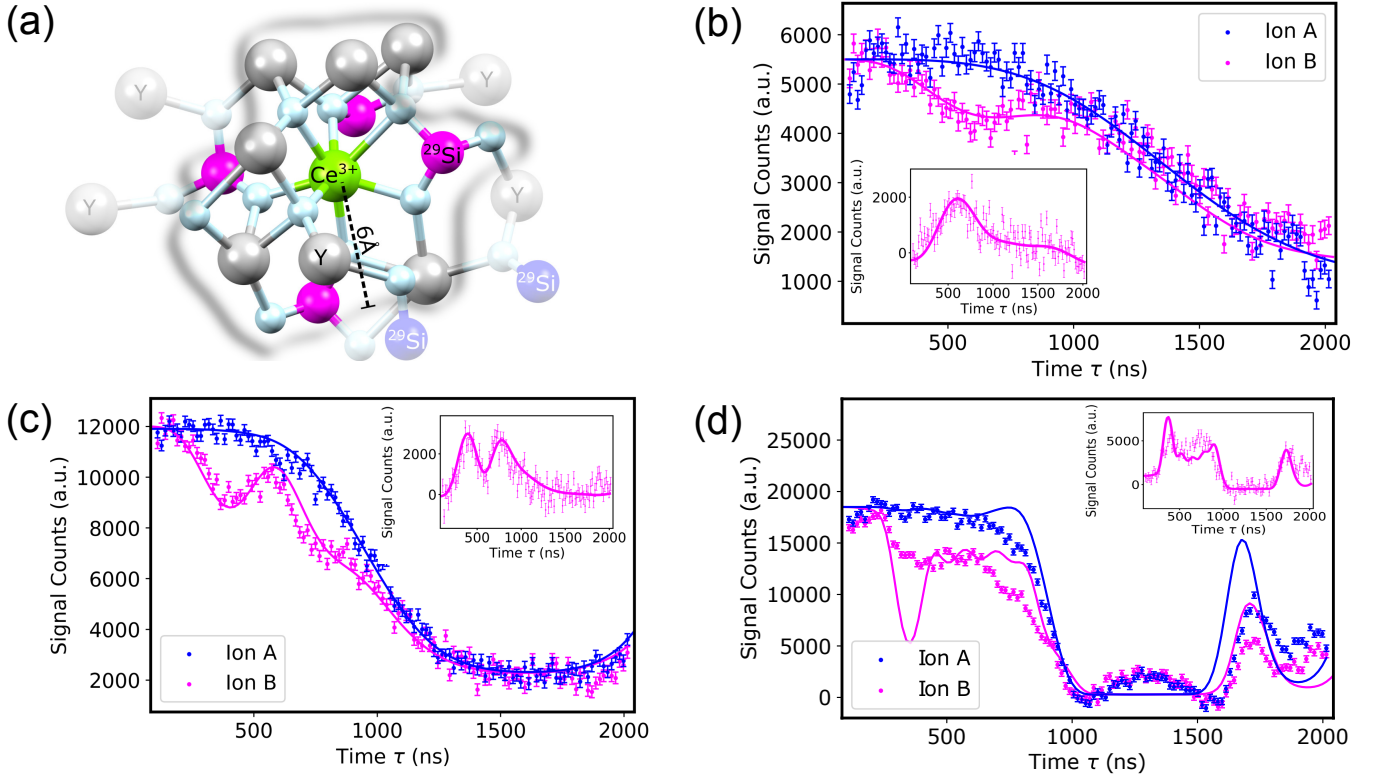


FIG. 4. (a) Schematic of the YSO crystal with embedded  $\text{Ce}^{3+}$ . Within 6 Å distance,  $^{29}\text{Si}$  coupling is detected (magenta), more remote  $^{29}\text{Si}$  cannot be distinguished (blue). (b)-(d) CPMG- $N$  decoupling sequences with varying number  $N$  of  $\pi$ -pulses. "Ion B" shows signal related to a  $^{29}\text{Si}$  nuclear spin close to the investigated  $\text{Ce}^{3+}$  ion. "Ion A" shows no  $^{29}\text{Si}$  signature. Solid lines come from ab-initio simulations of the corresponding DD sequences. (b) CPMG-1 (c) CPMG-2 (d) CPMG-5. Insets show differences between "ion A" and "ion B" data and simulations and represents only the silicon signal without overlapping yttrium modulation.

shown in Fig. 5). The cold-finger is connected to the heat-exchanger, where also the temperature measurement is picked up. Due to low heat conductivity of the magnet between sample and cold-finger, the cooling power is insufficient for thermalizing the YSO sample to the indicated temperature of  $T = 4\text{ K}$ , but rather to  $T_{\text{sample}} = 8\text{ K}$ . For rough positioning, the cold-finger is mounted on a 3D stage covering  $10\text{ mm} \times 10\text{ mm} \times 10\text{ mm}$ . To obtain high resolution fluorescence images, the objective lens, mounted on a 3D piezo stage (NPoint, NPXY100Z25-264) in the cryostat vacuum chamber, can be positioned throughout  $100\text{ }\mu\text{m} \times 100\text{ }\mu\text{m} \times 25\text{ }\mu\text{m}$  with nanometer resolution.

In order to obtain a picosecond-pulsed laser at around 355 nm wavelength, we used a dye laser cavity, which was synchronously pumped by a 532 nm picosecond pulsed Vanguard laser (Spectra-Physics) with 2W output power and 86 MHz repetition rate. The pumped Pyridin 1 dye radiation emitting at 710 nm was extracted from the laser cavity by an intra-cavity, externally triggerable Quartz AOM. With a BBO doubling crystal, we converted the pulsed 710 nm radiation into 355 nm and sent it through a single-mode polarization maintaining (Thorlabs, PANDA

PM-S350-HP) fiber for geometric mode cleaning. The linearly polarized light after the output of the fiber was then sent through a  $\lambda/4$  waveplate. It was found, that optical polarization fidelity of  $\text{Ce}^{3+}$  was not maximum at  $45^\circ$  tilt-angle of the  $\lambda/4$  waveplate, corresponding to perfectly circularly polarized light, but rather at slightly smaller tilt-angles of  $40^\circ$ , corresponding to slightly elliptically polarized light. This can originate from birefringence of the YSO crystal and also the 355 nm notch filter, used as a dichroic mirror in the confocal microscope setup, both capable to distort the polarization of light, which would have to be compensated. The fluorescence of  $\text{Ce}^{3+}$  was filtered with a 450 nm shortpass filter, in order to reject parasitic emission from impurities found in the YSO crystal, potentially originating from other RE ion species. Additionally, fluorescence was filtered by a  $10\text{ }\mu\text{m}$  pinhole, in order to increase the depth resolution of the microscope, before it was collected by a Photomultiplier Tube (Hamamatsu, H10682-210).

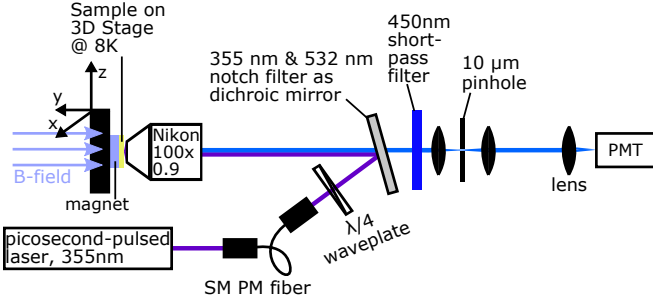


FIG. 5. Laser Scanning Confocal Microscope Setup. PMT: Photomultiplier Tube, SM PM fiber: single-mode polarization maintaining fiber.

## SUPERRESOLUTION MICROSCOPY

Based on similar optical properties of  $\text{Ce}^{3+}:\text{YAG}$  and  $\text{Ce}^{3+}:\text{YSO}$ , superresolution microscopy techniques, such as STED microscopy, which are known to be applicable to  $\text{Ce}^{3+}:\text{YAG}$ [24], were used to increase spatial resolution for microscopy of  $\text{Ce}^{3+}:\text{YSO}$ . This was achieved by superimposing a picosecond-pulsed 532 nm doughnut shaped depletion beam on the picosecond-pulsed 355 nm excitation beam. In order to obtain highest increase in optical resolution, laser powers had to be adjusted carefully with respect to each other and the 532 nm laser pulse arrival time had to be delayed with respect to the excitation pulse. The optical detection window for confocal laser scans for both, with and without additional STED beam, stayed unchanged throughout the experiments, and spanned the range between 365 nm-450 nm, as indicated in the left image of Fig. 6. Confocal laser scans depicted on the right side of Fig. 6 show on top the measurement without STED beam and on bottom with STED beam. By comparing individual point spread functions in both scans, we can quantify a resolution enhancement of factor 2. This resolution enhancement, though in principle capable of significantly reducing background noise for our spin spectroscopic studies, was not available in conjunction with spin manipulation. While the high power 532 nm depletion laser was used, no magnetic resonance signals could be acquired. We conjecture, that high power picosecond pulses at 532 nm prevent the optical spin initialization and readout, potentially through ionization of  $\text{Ce}^{3+}$  and surrounding traps.

## HAHN-ECHO MEASUREMENT SEQUENCE

For Hahn-Echo measurements, the signal was acquired in a balanced measurement sequence, where the final pulses in the sequence alternately projected the spin to  $|+1/2\rangle$  or  $| -1/2\rangle$ , by applying either  $\pi/2$  or  $3\pi/2$  MW pulses at the end of the sequence, depicted in Fig 7b. These two signals are subsequently subtracted from each

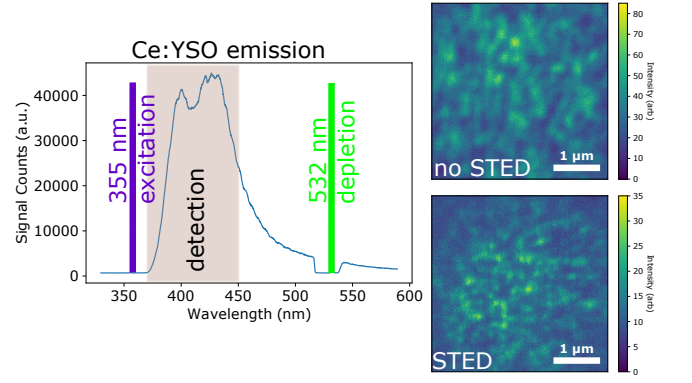


FIG. 6. STED microscopy of  $\text{Ce}^{3+}:\text{YSO}$ . Left side shows  $\text{Ce}^{3+}:\text{YSO}$  emission, superimposed with the spectral position of the picosecond pulsed 355 nm excitation laser, the picosecond pulsed 532 nm depletion laser and the spectral detection window for  $\text{Ce}^{3+}$  fluorescence. Right side shows two different confocal laser scans. Top image was taken without depletion laser, bottom image was taken with depletion laser.

other, which corresponds to the coherence of the electron spin at a time  $\tau$ , defined as the average value of the transverse spin component  $S_t = (|+1/2\rangle) - (|-1/2\rangle)$ .

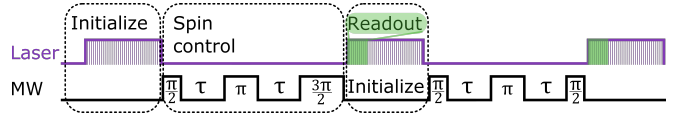


FIG. 7. Schematic diagram of the pulse sequence used for Hahn echo measurements, which show the difference between the  $3\pi/2$  MW pulse signal and the  $\pi/2$  MW pulse signal.

## SIMULATION

In this part, we give the simulation method of the spin decoherence of  $\text{Ce}^{3+}$  ion subjected to a YSO nuclear spin bath. The  $\text{Ce}^{3+}$  ion in the YSO crystal, substituting one yttrium, forms a defect center. Due to the crystal field, the fine structure of the  $\text{Ce}^{3+}$  ion splits further to three doublets. The ground doublet state subspace is our key concern. Its Hamiltonian is

$$H_{\text{Ce}} = \frac{\mu_B}{\hbar} \mathbf{B} \cdot g_{\text{eff}} \cdot \mathbf{S}, \quad (1)$$

where  $\mu_B$  is the Bohr magneton,  $\hbar$  is the Planck constant,  $\mathbf{B}$  is the magnetic field,  $\mathbf{S}$  is the lowest doublet state spin operator, and  $g_{\text{eff}}$  is the effective g-factor of  $\text{Ce}^{3+}$  [20, 34]

$$g_{\text{eff}} = \begin{pmatrix} 0.6514 & 0.2629 & 0.3004 \\ 0.2629 & 0.6799 & -0.0858 \\ 0.3004 & -0.0858 & 0.9098 \end{pmatrix}. \quad (2)$$

The  $\text{Ce}^{3+}$  ion is surrounded by a dense nuclear spin bath, which consists of  $^{89}\text{Y}$  nuclear spins and  $^{29}\text{Si}$  nuclear spins. These nuclear spins interact with  $\text{Ce}^{3+}$  ion through magnetic dipole-dipole interactions [25]

$$H_{\text{int}} = \sum_i \frac{\mu_B \mu_0 \gamma_i}{4\pi r_i^3} \mathbf{S} \cdot g_{\text{eff}} \cdot (3\mathbf{n}_i \mathbf{n}_i - \mathbb{I}) \cdot \mathbf{I}_i, \quad (3)$$

where  $\mu_0$  is the magnetic constant,  $\gamma_i$  is the gyromagnetic ratio of the  $i$ -th nuclear spin,  $\mathbf{I}_i$  is the  $i$ -th nuclear spin operator,  $r_i$  is the distance between the  $\text{Ce}^{3+}$  defect and the  $i$ -th nuclear spin, and  $\mathbf{n}_i$  is the corresponding unit vector. The nuclear spin bath itself is also governed by Hamiltonian

$$H_{\text{bath}} = \sum_i \gamma_i \mathbf{B} \cdot \mathbf{I}_i + \sum_{i>j} \frac{\mu_0 \gamma_i \gamma_j \hbar}{4\pi r_{ij}^3} \mathbf{I}_i \cdot (3\mathbf{n}_{ij} \mathbf{n}_{ij} - \mathbb{I}) \cdot \mathbf{I}_j, \quad (4)$$

where  $r_{ij}$  is the distance between two nuclear spins, and  $\mathbf{n}_{ij}$  is the corresponding unit vector.

Now, we investigate the decoherence of  $\text{Ce}^{3+}$  under the dynamical decoupling sequences CPMG- $N$ , where its decoherence is mainly contributed by its surrounding nuclear spins. In the experiment, we initialize the defect  $\text{Ce}^{3+}$  centers to a polarized state, and employ a microwave  $\pi/2$  pulse to prepare the defect  $\text{Ce}^{3+}$  to a coherence state. At experimental temperatures the nuclear spins are hardly polarized so that their initial state can be well modeled as a high-temperature mixed state  $\rho_{\text{bath}} = \otimes_{i=1}^N (\mathbb{I}_i / \text{Tr}[\mathbb{I}_i])$ , where  $\mathbb{I}_i$  is the identity operator for the  $i$ -th nuclear spin. Driven by the Hamiltonian  $H = H_{\text{Ce}} + H_{\text{bath}} + H_{\text{int}}$  under CPMG- $N$ , the decoherence of the defect centers can then be obtained as [25, 27]

$$L(2N\tau) = \text{Tr}_{\text{bath}} [e^{-iH-\tau} \dots e^{-iH+2\tau} e^{-iH-2\tau} \times e^{-iH+\tau} \rho_{\text{bath}} e^{iH-\tau} e^{iH+2\tau} e^{iH-2\tau} \dots e^{iH+\tau}], \quad (5)$$

where  $\tau$  is the pulse interval of the CPMG- $N$  sequences, and  $H_{\pm}$ , defined by

$$\begin{aligned} H_{\pm} &= \langle \pm | H_{\text{int}} + H_{\text{bath}} | \pm \rangle \\ &= H_{\text{bath}} \pm \frac{1}{2} \sum_i \frac{\mu_B \mu_0 \gamma_i}{4\pi r_i^3} \mathbf{n}_B \cdot (3\mathbf{n}_i \mathbf{n}_i - \mathbb{I}) \cdot \mathbf{I}_i, \end{aligned}$$

is the conditional Hamiltonian of  $H_{\text{int}} + H_{\text{bath}}$  projected to the eigenstate of  $H_{\text{Ce}} | \pm \rangle$  [25, 27]. With the help of Cluster-Correlation Expansion (CCE) method [27, 35], the decoherence of the  $\text{Ce}^{3+}$  is numerically calculated as

$$L(2N\tau) = \prod_{\{C\}} \tilde{L}_C(2N\tau), \quad (6)$$

where  $\tilde{L}_C(2N\tau)$  is the decoherence of  $\text{Ce}^{3+}$  induced by the nuclear spin cluster  $C$ . When the concerned

time scale is far less than microseconds (corresponding to interaction strength for single nuclear spins), the decoherence of the  $\text{Ce}^{3+}$  can be well described by a *non-interacting nuclear spin bath*. In our system, we can use such a non-interacting approximation because the Zeeman interaction strength and the hyperfine interaction strength between  $\text{Ce}^{3+}$  and the nuclear spins is much larger than the interaction within the bath spins.

As mentioned in the main text, the cerium density in the sample can lead to more than one  $\text{Ce}^{3+}$  ion to be probed within the focal volume. As a consequence, the decoherence signal can in principle result from more than one  $\text{Ce}^{3+}$  ion. The different  $\text{Ce}^{3+}$  ions in the same spot share the same yttrium nuclear spin environment. However, different  $\text{Ce}^{3+}$  ions can experience quite different  $^{29}\text{Si}$  nuclear spin environments, based on statistical occurrence of  $^{29}\text{Si}$ . To account for this, for simulations for "ion B" shown in Fig. (4) in the main text, we assumed there are two  $\text{Ce}^{3+}$  ions in a  $13 \times 5 \times 6 \text{ nm}^3$  lattice but only one  $\text{Ce}^{3+}$  ion has a proximal  $^{29}\text{Si}$  with distance 3.6 Å. While for "ion A", we assumed there is only one  $\text{Ce}^{3+}$  ion and no proximal  $^{29}\text{Si}$  nearby  $\text{Ce}^{3+}$  in a distance smaller than 6 Å. While we cannot distinguish between one or two coupled  $^{29}\text{Si}$  with distance closer than 6 Å to the  $\text{Ce}^{3+}$  ion with the demonstrated spin spectroscopy, it is more likely to sense exactly one single  $^{29}\text{Si}$  nuclear spin. Based on the 5% abundance of  $^{29}\text{Si}$ , we have estimated the likelihood to detect no  $^{29}\text{Si}$  at all, exactly one  $^{29}\text{Si}$  or two  $^{29}\text{Si}$ , shown in Figure 8.

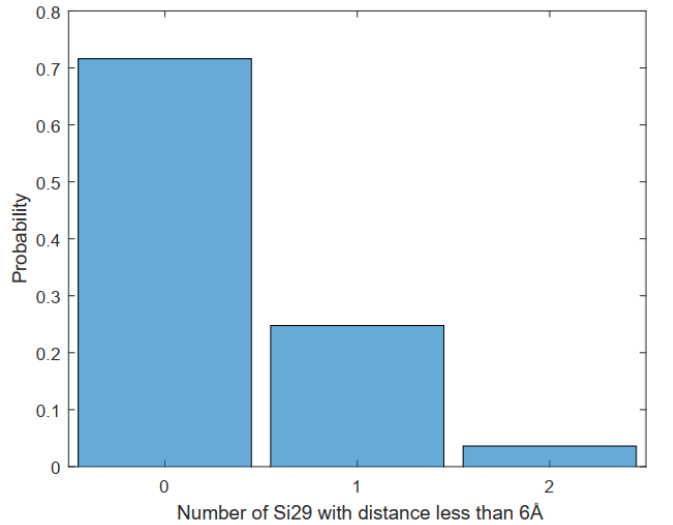


FIG. 8. Probability for a  $\text{Ce}^{3+}$  ion in YSO crystal to have a certain number of  $^{29}\text{Si}$  located at a distance smaller than 6 Å.

The coherence difference between two different ions reflects the difference from proximal  $^{29}\text{Si}$  nuclear spin environment. With increasing CPMG pulse number, we expect the coherence difference to have  $N$  sharp coherence dips via a direct CCE simulation. However, the experi-

mentally observed coherence dips are much more shallow than the theoretical prediction for CPMG-5. One possible reason is external noise for proximal  $^{29}\text{Si}$ , for example magnetic field fluctuations introduced by MW manipulation to  $\text{Ce}^{3+}$ . To take noise into account, we phenomenologically add a relaxation and dephasing mechanism to the dynamics of  $^{29}\text{Si}$  [30, 36, 37]

$$\dot{\rho} = \mathcal{L}_{\text{coh}}\rho + \gamma_2^{\text{Si}} (\sigma_{\text{Si}}^z \rho \sigma_{\text{Si}}^z - \rho) + \frac{\gamma_1^{\text{Si}}}{2} (\sigma_{\text{Si}}^x \rho \sigma_{\text{Si}}^x - \rho) + \frac{\gamma_1^{\text{Si}}}{2} (\sigma_{\text{Si}}^y \rho \sigma_{\text{Si}}^y - \rho), \quad (7)$$

where  $\mathcal{L}_{\text{coh}}\rho = -i[H, \rho]$ ,  $\sigma_{\text{Si}}^{x,y,z}$  are the Pauli matrices of the proximal  $^{29}\text{Si}$  nuclear spin, and  $\gamma_2^{\text{Si}}$  and  $\gamma_1^{\text{Si}}$  are the dephasing and relaxation rates. Our simulation, shown as solid lines in the main text in Fig. 4(b)-(d), uses  $\gamma_1^{\text{Si}} = \gamma_2^{\text{Si}} = 64 \text{ kHz}$  (which ranges at a similar magnitude in the NV center system [30]).

---

\* t.kornher@pi3.uni-stuttgart.de

- [1] J. Morton, A. M. Tyryshkin, R. M. Brown, S. Shankar, B. W. Lovett, A. Ardavan, T. Schenkel, E. E. Haller, J. W. Ager, and S. A. Lyon, *Nature* **455**, 1085 (2008).
- [2] P. C. Maurer, G. Kucsko, C. Latta, L. Jiang, N. Y. Yao, S. D. Bennett, F. Pastawski, D. Hunger, N. Chisholm, M. Markham, D. Twitchen, J. Cirac, and M. Lukin, *Science* **336**, 1283 (2012).
- [3] D. D. Awschalom, R. Hanson, J. Wrachtrup, and B. B. Zhou, *Nat. Photonics* **12**, 516 (2018).
- [4] G. Waldherr, Y. Wang, S. Zaiser, M. Jamali, T. Schulte-Herbrüggen, H. Abe, T. Ohshima, J. Isoya, J. Du, P. Neumann, and J. Wrachtrup, *Nature* **506**, 204 (2014).
- [5] A. M. Dibos, M. Raha, C. M. Phenicie, and J. D. Thompson, *Phys. Rev. Lett.* **120**, 243601 (2018).
- [6] H. De Riedmatten and M. Afzelius, in *Engineering the Atom-Photon Interaction* (Springer, 2015) pp. 241–273.
- [7] M. Zhong, M. P. Hedges, R. L. Ahlefeldt, J. G. Bartholomew, S. E. Beavan, S. M. Wittig, J. J. Longdell, and M. J. Sellars, *Nature* **517**, 177 (2015).
- [8] R. Kolesov, K. Xia, R. Reuter, R. Stöhr, A. Zappe, J. Meijer, P. Hemmer, and J. Wrachtrup, *Nat. Commun.* **3**, 1029 (2012).
- [9] C. Yin, M. Rancic, G. G. de Boo, N. Stavrias, J. C. McCallum, M. J. Sellars, and S. Rogge, *Nature* **497**, 91 (2013).
- [10] R. Kolesov, K. Xia, R. Reuter, M. Jamali, R. Stöhr, T. Inal, P. Siyushev, and J. Wrachtrup, *Phys. Rev. Lett.* **111**, 120502 (2013).
- [11] T. Zhong, J. M. Kindem, J. G. Bartholomew, J. Rochman, I. Craiciu, V. Verma, S. W. Nam, F. Marsili, M. D. Shaw, A. D. Beyer, and A. Faraon, *Phys. Rev. Lett.* **121**, 183603 (2018).
- [12] N. Zhao, J. Honert, B. Schmid, M. Klas, J. Isoya, M. Markham, D. Twitchen, F. Jelezko, R.-B. Liu, H. Fedder, and J. Wrachtrup, *Nat. Nanotechnol.* **7**, 657 (2012).
- [13] S. Kolkowitz, Q. P. Unterreithmeier, S. D. Bennett, and M. D. Lukin, *Phys. Rev. Lett.* **109**, 137601 (2012).
- [14] T. H. Taminiau, J. J. T. Wagenaar, T. van der Sar, F. Jelezko, V. V. Dobrovitski, and R. Hanson, *Phys. Rev. Lett.* **109**, 137602 (2012).
- [15] B. Car, L. Veissier, A. Louchet-Chauvet, J.-L. Le Gouët, and T. Chanelière, *Phys. Rev. Lett.* **120**, 197401 (2018).
- [16] M. Zhong, R. L. Ahlefeldt, and M. J. Sellars, *New J. Phys.* **21**, 033019 (2019).
- [17] L. Childress, M. G. Dutt, J. Taylor, A. Zibrov, F. Jelezko, J. Wrachtrup, P. Hemmer, and M. Lukin, *Science* **314**, 281 (2006).
- [18] R. Nagy, M. Niethammer, M. Widmann, Y.-C. Chen, P. Udvarhelyi, C. Bonato, J. U. Hassan, R. Karhu, I. G. Ivanov, N. T. Son, *et al.*, *Nat. Commun.* **10**, 1954 (2019).
- [19] J. J. Pla, K. Y. Tan, J. P. Dehollain, W. H. Lim, J. J. Morton, F. A. Zwanenburg, D. N. Jamieson, A. S. Dzurak, and A. Morello, *Nature* **496**, 334 (2013).
- [20] L. Pidot, O. Guillot-Noël, A. Kahn-Harari, B. Viana, D. Pelenc, and D. Gourier, *J. Phys. Chem. Solids* **67**, 643 (2006).
- [21] W. Drozdowski, A. J. Wojtowicz, D. Wiśniewski, P. Szupryczyński, S. Janus, J.-L. Lefaucheur, and Z. Gou, *J. Alloys Compd.* **380**, 146 (2004).
- [22] , Supplementary Material.
- [23] Y. Yan, J. Karlsson, L. Rippe, A. Walther, D. Serrano, D. Lindgren, M.-e. Pistol, S. Kröll, P. Goldner, L. Zheng, and J. Xu, *Phys. Rev. B* **87**, 184205 (2013).
- [24] R. Kolesov, S. Lasse, C. Rothfuchs, A. D. Wieck, K. Xia, T. Kornher, and J. Wrachtrup, *Phys. Rev. Lett.* **120**, 033903 (2018).
- [25] P. Siyushev, K. Xia, R. Reuter, M. Jamali, N. Zhao, N. Yang, C. Duan, N. Kukharchyk, A. Wieck, R. Kolesov, and J. Wrachtrup, *Nat. Commun.* **5**, 3895 (2014).
- [26] A. Schweiger and G. Jeschke, in *Principles of Pulse Electron Paramagnetic Resonance* (Oxford University Press, 2001) pp. 247–255.
- [27] N. Zhao, S.-W. Ho, and R.-B. Liu, *Phys. Rev. B* **85**, 115303 (2012).
- [28] I. Kurkin and K. Chernov, *Physica B+C* **101**, 233 (1980).
- [29] N. Zhao, J.-L. Hu, S.-W. Ho, J. T. Wan, and R. Liu, *Nat. Nanotechnol.* **6**, 242 (2011).
- [30] P. Wang and W. Yang, *New J. Phys.* **17**, 113041 (2015).
- [31] W. Ma, F. Shi, K. Xu, P. Wang, X. Xu, X. Rong, C. Ju, C.-K. Duan, N. Zhao, and J. Du, *Phys. Rev. A* **92**, 033418 (2015).
- [32] P. London, J. Scheuer, J.-M. Cai, I. Schwarz, A. Retzker, M. B. Plenio, M. Katagiri, T. Teraji, S. Koizumi, J. Isoya, R. Fischer, L. P. McGuinness, B. Naydenov, and F. Jelezko, *Phys. Rev. Lett.* **111**, 067601 (2013).
- [33] M. Raha, S. Chen, C. M. Phenicie, S. ourari, A. M. Dibos, and J. Thompson, *arXiv.org arXiv:1907.09992v1* (2019).
- [34] J. Wen, C.-K. Duan, L. Ning, Y. Huang, S. Zhan, J. Zhang, and M. Yin, *J. Phys. Chem. A* **118**, 4988 (2014).
- [35] W. Yang and R.-B. Liu, *Phys. Rev. B* **79**, 115320 (2009).
- [36] G. Lindblad, *Comm. Math. Phys.* **48**, 119 (1976).
- [37] H.-P. Breuer and F. Petruccione, *The Theory of Open Quantum Systems* (Oxford University Press, 2002).